Turbulence modeling for separated flow

By P. A. Durbin

1. Motivation and objectives

Two projects are described in this report. The first involves assessing turbulence models in separated flow. The second addresses the anomalous behavior of certain turbulence models, such as $k-\varepsilon$, in stagnation point flow.

The primary motivation for developing turbulent transport models is to provide tools for computing non-equilibrium, or complex, turbulent flows. Simple flows can be analyzed using data correlations or algebraic eddy viscosities, but in more complicated flows such as a massively separated boundary layer, a more elaborate level of modeling is required. It is widely believed that at least a two-equation transport model is required in such cases. The transport equations determine the evolution of suitable velocity and time-scales of the turbulence. The appropriate velocity scale for turbulent transport toward a wall is the normal component, $\overline{v^2}$, not the turbulent intensity, k. This and other considerations motivated the $k-\varepsilon-v^2$ model, which can be used in wall-bounded flows. Applications to complex geometry require a generalized interpretation of the velocity scale $\overline{v^2}$. The model originally was developed for attached or mildly separated boundary layers. Rather promising results were obtained in tests of the formulation. Here the model is assessed in strongly separated flows. Doing so requires that $\overline{v^2}$ be regarded simply as a velocity scale that satisfies boundary conditions suitable for the normal component of turbulent intensity; it cannot be regarded as the 'y-component' because that would be inappropriate in general geometries that can have surfaces aligned in any direction. This loosened understanding of $\overline{v^2}$ presents no operational difficulties.

Two equation models as well as the $k-\varepsilon-v^2$ model predict an anomalously large growth of turbulent kinetic energy in stagnation point flows. Even when the stagnation point region is not of interest *per se*, this spurious behavior can upset the rest of the flow computation. A formal upper limit to the turbulent time-scale in such models alleviates their stagnation point anomaly. This bound is derived in §2.4 and is illustrated with the stagnation point flow at the leading edge of an airfoil.

2. Accomplishments

The governing equations of the $k-\varepsilon-v^2$ model will not be presented here. Their initial development is described in Durbin (1991), and a more complete description of the present work will appear in Durbin (1994). The mean flow satisfies the incompressible Navier-Stokes equations with an eddy viscosity. The turbulence model uses the standard $k-\varepsilon$ equations, a $\overline{v^2}$ transport equation and an elliptic relaxation equation for the source term f_{22} in the $\overline{v^2}$-equation.

The computations were done with an extended version of the INS2D code of Rogers and Kwak (1990). The extensions required for the present computations

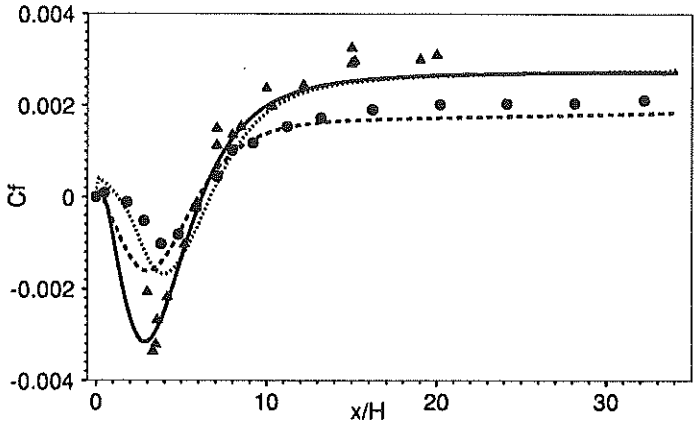

FIGURE 1. Skin friction coefficient on wall downstream of the backstep compared to experiments of Jovic and Driver (——— , ▲) and Driver and Seegmiller (---- , ●). ····· line is solution to SSG model for Jovic and Driver flow.

consist of providing subroutines to solve the transport and elliptic relaxation equations of the $k-\varepsilon-v^2$ model. This code development will not be described here. The numerics are discussed in Durbin (1994). The program can solve full second moment closure models as well as eddy viscosity models.

The present study included assessment of second-moment closures in separated flow. The results were generally less satisfactory than $k-\varepsilon-v^2$. These second-moment computations will not be presented.

Sections 2.1–2.3 present three separated flows: these illustrate sharp edge separation; smooth wall, pressure driven separation; and unsteady vortex shedding. This last case was studied at the suggestion of colleagues at Pratt & Whitney.

2.1 Flow over backward facing steps

The backstep flow configurations studied experimentally by Jovic and Driver (1993) and by Driver and Seegmiller (1985) were computed with the $k-\varepsilon-v^2$ model and with second-moment closure models. The JD experiment had a step height Reynolds number of 5,000; the DS case had $Re = 37,500$. Both the IP and SSG second-moment closures as incorporated into the elliptic relaxation procedure were tried. Computations showed that they significantly under-predict the magnitude of the reversed flow downstream of the step, as suggested by the dotted skin friction curve in Fig. 1: this should be compared to the solid line and triangles.

Computed and experimental skin friction coefficients on the wall downstream of the step are compared in Fig. 1. The computed reattachment point at $x = 6.2$ step heights is in agreement with the data. The relatively large negative skin friction in the JD experiment is due to low Reynolds number. The $k-\varepsilon-v^2$ model correctly shows this sensitivity to Reynolds number. Overall, the agreement with experiment is better than has been found using the standard $k-\varepsilon$ model with wall functions (Driver and Seegmiller, 1985); numerous independent computations have shown

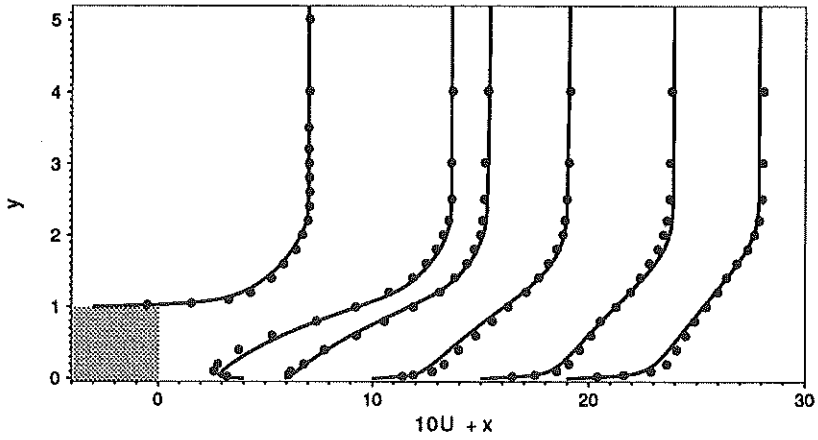

FIGURE 2. Mean velocity profiles for the Jovic and Driver experiment.

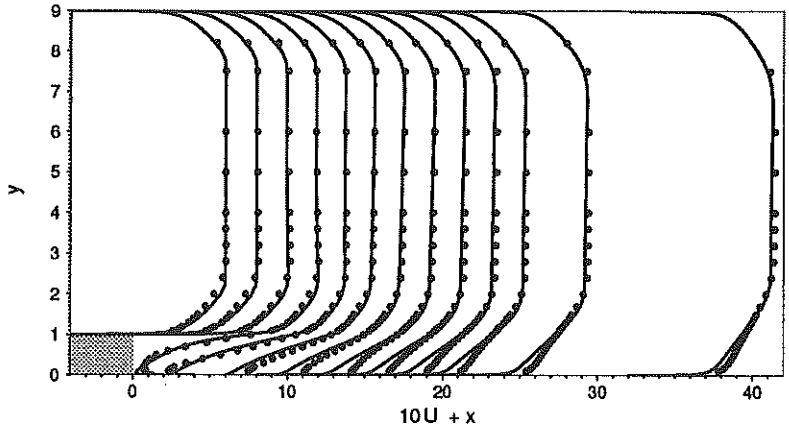

FIGURE 3. Mean velocity profiles for the Driver and Seegmiller experiment.

that model under-predicts the reattachment length.

Figs. 2 and 3 show profiles of the U-component of velocity. These profiles are plotted in the form $10U + x$ to display their evolution down the duct. The agreement between model and experiment in the JD case is quite good. In the higher Reynolds number DS case, the agreement is good for $x < 8$, but the model solution for the boundary layer downstream of reattachment recovers more slowly than the data. This slow recovery downstream of reattachment is a universal problem of turbulence models shown by Reynolds stress as well as $k - \varepsilon$ models.

2.2 A separated diffuser

Obi *et al.* (1993) measured the flow in a one-sided, 10° plane diffuser. The expansion ratio of 4.7 was sufficient to produce a separation bubble on the sloping wall; hence, this provides a test case for smooth, adverse pressure driven separation. The entrance to the diffuser consisted of a long plane channel (aspect ratio 35) in

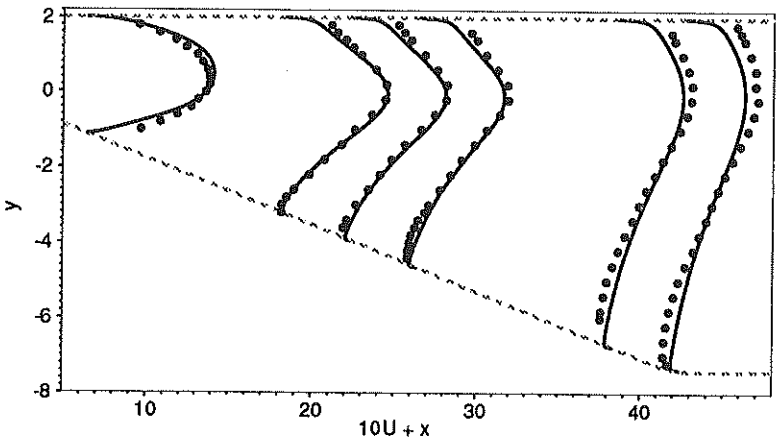

FIGURE 4. Mean velocity profiles in the Obi, *et al.* diffuser. Both Eq. (9) (———) and a constant value of 1.55 (----) were used for $C^z_{\varepsilon_1}$. The light dashed lines show the diffuser surface.

order to produce fully developed flow. The Reynolds number based on the half-height of this channel was 10,000. The computational inflow profiles were obtained by solving fully developed channel flow with a parabolic code. Fig. 4 shows profiles of $10U + x$. The boundary of the diffuser is indicated in the figure—note, however, that the aspect ratio of this figure is not unity: the actual duct is more elongated. The profiles on the ramp are in good agreement with the data, showing the smooth separation; further downstream, the predicted backflow is less strong than the data. Note that the mass flux is constant, so less backflow near the lower wall is necessarily accompanied by less forward flow in the upper part of the channel. Second moment closure computations of this flow failed to predict the separation in this flow. Both SSG and IP second-moment closure models gave only a tiny region of reversed flow at the foot of the ramp.

2.3 Vortex shedding behind a triangular cylinder

The flow around a triangular cylinder in a duct was measured by Sjunnesson (presented in Johansson *et al.* 1993). This geometry provides an example of bluff body flow with fixed separation points. The study by Sjunnesson was motivated by the application to flame holders. The geometry consists of a 6:1 aspect ratio equilateral triangular cylinder centered symmetrically in a duct three cylinder sides high. The Reynolds number based on the cylinder side and inlet velocity was about 42,500.

Both steady state and (statistically) unsteady solutions were computed. By taking a large artificial time-step on the order of the shedding period in length, we obtained symmetric, steady solutions. Upon introducing an asymmetric disturbance and taking a smaller step, an oscillatory solution was obtained. Fig. 5 is a composite showing the time-averaged U-contours of the unsteady computation in the upper half and the steady state solution in the lower. It shows that the steady-state

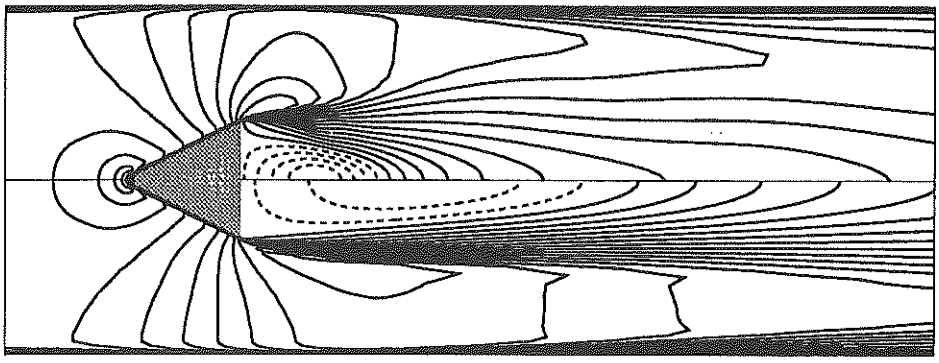

FIGURE 5. U-contours for a steady calculation (lower half) and time-average of an unsteady computation with vortex shedding (upper half).

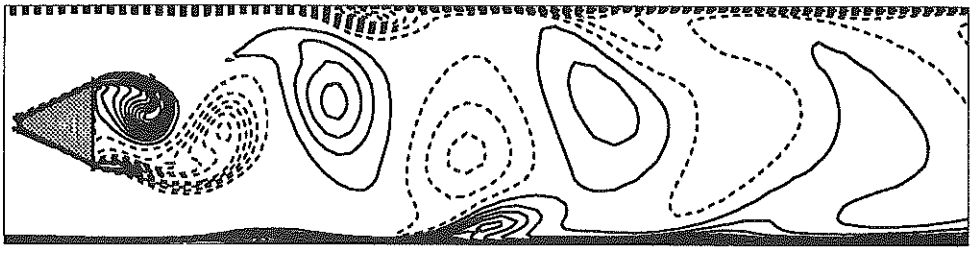

FIGURE 6. Instantaneous vorticity contours showing shedding in the time accurate computation.

separation bubble is over twice as long as the averaged, unsteady bubble.

Instantaneous vorticity contours, in Fig. 6, show the asymmetric flow in the time accurate computation. The interaction between the vortex street and the boundary layers in the side walls results in eruption of secondary vorticity. The complexity of such interactions underscores the need to resolve the coherent vortices in this type of flow.

Fig. 7 shows profiles of the time-averaged U-velocity component in the wake. The computational results were obtained by averaging the numerical solution over one period of the vortex shedding. The profiles are displayed evenly spaced, but the actual locations were $x = 0.375$, 0.95, 1.525, 3.75, and 9.4 heights downstream of the rear face of the cylinder. The agreement between experiment and model is excellent. The first profile at $x = 0.375$ shows the sharp boundary and large velocity deficit of the near wake. By $x = 0.95$ the wake profile has altered substantially and is undergoing transition to a Gaussian form. The different curves show the convergence of the solution with grid refinement. It can be concluded that the

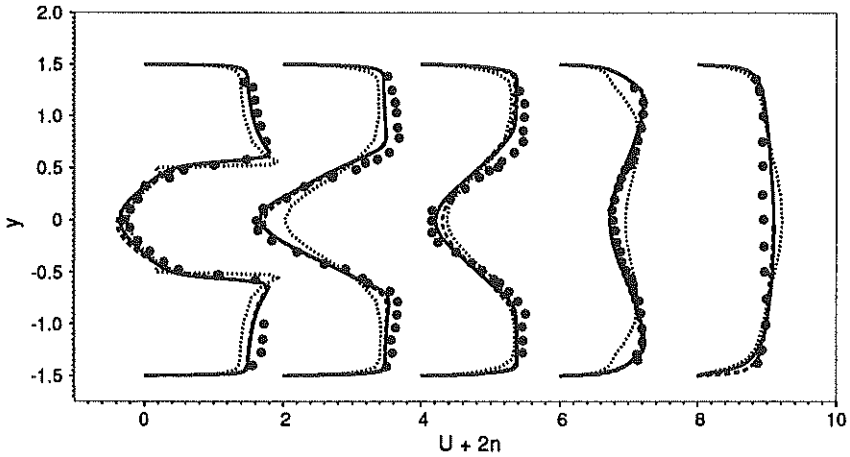

FIGURE 7. Time-averaged velocity profiles in the wake of a triangular cylinder. The calculations are shown for three grids: 141 × 101 (——), 121 × 91 (----); 71 × 51 (·····)

statistical unsteadiness produced by vortex shedding must be resolved in order to compute this flow. The steady state computation of this flow is as dubious as a homogeneous computation of a spatially homogeneous flow; it leads to quite erroneous predictions.

2.4 On the $k-\varepsilon$ stagnation point anomaly

Two equation models as well as $k-\varepsilon-v^2$ predict an anomalously large growth of turbulent kinetic energy near to stagnation points (Launder and Kato, 1993; Menter, 1992). This can cause difficulties in aerodynamic flows with a free-stream impinging on a blunt leading edge. Even when the stagnation point region is not of interest *per se*, this spurious behavior can upset the rest of the flow computation. The usual explanation for the stagnation point anomaly is that the eddy viscosity formula

$$\overline{u_i u_j} = -2\nu_t S_{ij} + \frac{2}{3}k\delta_{ij} \tag{1}$$

gives an erroneous normal stress difference (Launder and Kato 1993). In (1), $S_{ij} = (\partial_i U_j + \partial_j U_i)/2$ is the rate of strain and

$$\nu_t = C_\mu k T \tag{2}$$

is the eddy viscosity. T is the turbulent time-scale (e.g., k/ε).

Some of our computations suggest an alternative understanding of the anomaly: as the stagnation point is approached, T becomes very large. The ε-equation is of the form

$$\partial_t \varepsilon + U \cdot \nabla \varepsilon = \frac{C_{\varepsilon_1}\mathcal{P} - C_{\varepsilon_2}\varepsilon}{T} + \nabla \cdot \left((\nu + \frac{\nu_t}{\sigma_\varepsilon})\nabla \varepsilon \right), \tag{3}$$

where the rate of turbulent energy production is $\mathcal{P} = 2\nu_t S_{ij} S_{ji}$. A large value of T in Eq. (3) causes the production of ε to be too small, allowing spuriously high turbulent kinetic energy. The stagnation point anomaly can be ameliorated by imposing a bound on the time-scale. In the following we will derive the constraint

$$T = \min\left(\frac{k}{\varepsilon}, \frac{2}{3C_\mu}\sqrt{\frac{3}{8|\mathbf{S}|^2}}\right). \tag{4}$$

where $S_{ij}S_{ji} \equiv |\mathbf{S}|^2$. In most situations this reduces to $T = k/\varepsilon$; in highly strained flow the upper bound comes into play.

The constraint will be derived by requiring that (1) satisfy $2k \geq \overline{u^2} \geq 0$, which can be called a 'realizability condition'. The rate of strain tensor S_{ij} is symmetric and becomes purely diagonal in principal-axes coordinates. The diagonal elements, λ_α, $\alpha = 1 \ldots 3$, are its eigenvalues and satisfy

$$\lambda_1^2 + \lambda_2^2 + \lambda_3^2 = |\mathbf{S}|^2. \tag{5}$$

In incompressible flow

$$\lambda_1 + \lambda_2 + \lambda_3 = 0 \tag{6}$$

It follows from (5) and (6) that

$$|\lambda_\alpha| = \sqrt{|\mathbf{S}|^2/2} \tag{7}$$

in two dimensions (i.e., when $\lambda_3 = 0$), and

$$|\lambda_\alpha| \leq \sqrt{2|\mathbf{S}|^2/3} \tag{8}$$

in three dimensions.

If (1) is written in the principal axes of S_{ij}, it becomes

$$\overline{u_\alpha^2} = -2\nu_t\lambda_\alpha + \frac{2}{3}k. \tag{9}$$

Of the constrains $\overline{u_\alpha^2} \geq 0$ and $2k \geq \overline{u_\alpha^2}$, $\forall\,\alpha$, the former is more stringent; this constraint is

$$2\nu_t \max_\alpha \lambda_\alpha \leq \frac{2}{3}k. \tag{10}$$

Substituting (2) into (11) results in the time-scale bound

$$T \leq \frac{1}{3C_\mu}\frac{1}{\max\lambda_\alpha} \tag{11}$$

which gives

$$T \leq \frac{2}{3C_\mu}\frac{1}{\sqrt{2|\mathbf{S}|^2}} \tag{12}$$

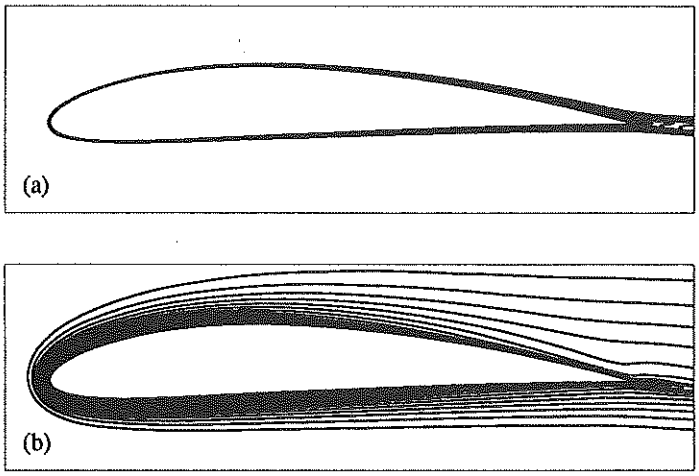

FIGURE 8. Contours of constant k/U_∞^2: (a), with (6) imposed; (b), without constraint. Contour intervals of 1.5×10^{-3}.

in two dimensions, and

$$T \leq \frac{2}{3C_\mu}\sqrt{\frac{3}{8|\mathbf{S}|^2}} \tag{13}$$

in three dimensions. These bounds might be imposed computationally by Eq. 4.

Fig. 8 shows k contours for the flow over a NACA4412 airfoil at zero angle of attack and with $k = 4 \times 10^{-4}\, U_\infty^2$ in the approach flow, with and without the constraint on T. This computation was done with the $k-\varepsilon-v^2$ model. The constraint prevents the spurious growth of k although some amplification still occurs.

3. Future plans

Flows with mean swirl are of interest for their role in enhancing mixing both by turbulent and mean motion. The swirl can have a stabilizing as well as a destabilizing effect on the turbulence. I have written an axi-symmetric extension to the INS-2D computer program and added the capability to compute swirling flow. This is in order to study confined coaxial jets with or without swirl. High swirl can produce vortex breakdown on the centerline of the jet. This type of flow occurs in various combustors.

The present vortex shedding calculations suggest that the application of turbulence models to separation control by external periodic excitation should be explored. This is a problem that Hans Kaltenbach has been investigating by LES.

REFERENCES

DRIVER, D. & SEEGMILLER, H. L. 1985 Features of a reattaching turbulent shear layer in divergent channel flow. *AIAA Journal.* **23,** 163–171.

DURBIN, P. A. 1991 Near-wall turbulence closure modeling without 'damping functions'. *Theoret. Comput. Fluid Dynamics.* **3,** 1–13.

DURBIN, P. A. 1994 Separated flow computations with the $k-\varepsilon-v^2$ model. *AIAA Journal.* To appear.

JOHANSSON, S., DAVIDSON, L. & OLSSON, E. 1993 Numerical simulation of the vortex shedding past triangular cylinders at high Reynolds number using a $k-\varepsilon$ turbulence model. *Int. J. Num. Meth. Fluids.* **16,** 859–878.

JOVIC, S. & DRIVER, D. 1993 Backward-facing step measurements at low Reynolds number, private communication.

LAUNDER, B. E. & KATO, M. 1993 Modelling flow-induced oscillations in turbulent flow around a square cylinder. *ASME-FED.* **157,** 189–199

MENTER, F. R. 1992 Improved two-equation $k-\omega$ models for aerodynamic flows. *NASA TM.* **103975.**

OBI, S., OHIMUZI, H., AOKI, K.& MASUDA, S. 1993 Experimental and computational study of turbulent separating flow in an asymmetric plane diffuser, 9th *Symp. on Turbulent Shear Flows*, Kyoto, Japan.

ROGERS, S. E. & KWAK, D. 1990 Upwind differencing scheme for the time-accurate incompressible Navier-Stokes equations. *AIAA Journal.* **28,** 253–262.